Use this document as a template

My PhD Thesis

Customise this page according to your needs

Tobias Hangleiter*

May 25, 2025

* A LaTeX lover/hater

The harmony of the world is made manifest in Form and Number, and the heart and soul and all the poetry of Natural Philosophy are embodied in the concept of mathematical beauty.

– D'Arcy Wentworth Thompson

Contents

List of Figures

Publications

[1] Yaiza Aragonés-Soria, René Otten, Tobias Hangleiter, Pascal Cerfontaine, and David Gross. "Minimising Statistical Errors in Calibration of Quantum-Gate Sets." June 7, 2022. DOI: `10.48550/arXiv.2206.03417`. (Visited on 06/08/2022). Pre-published.

[2] Pascal Cerfontaine, Tobias Hangleiter, and Hendrik Bluhm. "Filter Functions for Quantum Processes under Correlated Noise." In: *Phys. Rev. Lett.* 127.17 (Oct. 18, 2021), p. 170403. DOI: `10.1103/PhysRevLett.127.170403`.

[3] Thomas Descamps, Feng Liu, Sebastian Kindel, René Otten, Tobias Hangleiter, Chao Zhao, Mihail Ion Lepsa, Julian Ritzmann, Arne Ludwig, Andreas D. Wieck, Beata E. Kardynał, and Hendrik Bluhm. "Semiconductor Membranes for Electrostatic Exciton Trapping in Optically Addressable Quantum Transport Devices." In: *Phys. Rev. Appl.* 19.4 (Apr. 28, 2023), p. 044095. DOI: `10.1103/PhysRevApplied.19.044095`. (Visited on 04/28/2023).

[4] Thomas Descamps, Feng Liu, Tobias Hangleiter, Sebastian Kindel, Beata E. Kardynał, and Hendrik Bluhm. "Millikelvin Confocal Microscope with Free-Space Access and High-Frequency Electrical Control." In: *Review of Scientific Instruments* 95.8 (Aug. 9, 2024), p. 083706. DOI: `10.1063/5.0200889`. (Visited on 08/12/2024).

[5] Denny Dütz, Sebastian Kock, Tobias Hangleiter, and Hendrik Bluhm. "Distributed Bragg Reflectors for Thermal Isolation of Semiconductor Spin Qubits."

[6] Sarah Fleitmann, Fabian Hader, Jan Vogelbruch, Simon Humpohl, Tobias Hangleiter, Stefanie Meyer, and Stefan van Waasen. "Noise Reduction Methods for Charge Stability Diagrams of Double Quantum Dots." In: *IEEE Trans. Quantum Eng.* 3 (2022), pp. 1–19. DOI: `10.1109/TQE.2022.3165968`.

[7] Fabian Hader, Jan Vogelbruch, Simon Humpohl, Tobias Hangleiter, Chimezie Eguzo, Stefan Heinen, Stefanie Meyer, and Stefan van Waasen. "On Noise-Sensitive Automatic Tuning of Gate-Defined Sensor Dots." In: *IEEE Trans. Quantum Eng.* 4 (2023), pp. 1–18. DOI: `10.1109/TQE.2023.3255743`.

[8] Tobias Hangleiter, Pascal Cerfontaine, and Hendrik Bluhm. "Filter-Function Formalism and Software Package to Compute Quantum Processes of Gate Sequences for Classical Non-Markovian Noise." In: *Phys. Rev. Research* 3.4 (Oct. 18, 2021), p. 043047. DOI: `10.1103/PhysRevResearch.3.043047`. (Visited on 01/19/2022).

[9] Tobias Hangleiter, Pascal Cerfontaine, and Hendrik Bluhm. "Erratum: Filter-function Formalism and Software Package to Compute Quantum Processes of Gate Sequences for Classical Non-Markovian Noise [Phys. Rev. Research 3, 043047 (2021)]." In: *Phys. Rev. Res.* 6.4 (Oct. 16, 2024), p. 049001. DOI: `10.1103/PhysRevResearch.6.049001`. (Visited on 10/16/2024).

[10] Isabel Nha Minh Le, Julian D. Teske, Tobias Hangleiter, Pascal Cerfontaine, and Hendrik Bluhm. "Analytic Filter-Function Derivatives for Quantum Optimal Control." In: *Phys. Rev. Applied* 17.2 (Feb. 2, 2022), p. 024006. DOI: `10.1103/PhysRevApplied.17.024006`. (Visited on 02/03/2022).

[11] Paul Surrey, Julian D. Teske, Tobias Hangleiter, Pascal Cerfontaine, and Hendrik Bluhm. "Data-Driven Qubit Characterization and Optimal Control Using Deep Learning."

[12] Kui Wu, Sebastian Kindel, Thomas Descamps, Tobias Hangleiter, Jan Christoph Müller, Rebecca Rodrigo, Florian Merget, Beata E. Kardynal, Hendrik Bluhm, and Jeremy Witzens. "Modeling an Efficient Singlet-Triplet-Spin-Qubit-to-Photon Interface Assisted by a Photonic Crystal Cavity." In: *Phys. Rev. Appl.* 21.5 (May 24, 2024), p. 054052. DOI: `10.1103/PhysRevApplied.21.054052`. (Visited on 08/21/2024).

Software

The following open-source software packages were developed (at least partially) during the work on this thesis.

[1] Tobias Hangleiter, Isabel Nha Minh Le, and Julian D. Teske, *Filter_functions* version v1.1.3, May 14, 2024. Zenodo. DOI: 10.5281/ZENODO.4575000.

[2] Tobias Hangleiter, *Lindblad_mc_tools*.

[3] Tobias Hangleiter, *Mjolnir*.

[4] Tobias Hangleiter, Simon Humpohl, Max Beer, and René Otten, *Python-Spectrometer* version 2024.11.1, Nov. 21, 2024. Zenodo. DOI: 10.5281/ZENODO.13789861.

[5] Tobias Hangleiter, Simon Humpohl, Paul Surrey, and Han Na We, *Qutil* version 2024.11.1, Nov. 21, 2024. Zenodo. DOI: 10.5281/ZENODO.14200303.

Part I

A Flexible Python Tool For Fourier-Transform Noise Spectroscopy

Part II

Characterization and Improvements of a Millikelvin Confocal Microscope

Introduction | 1

N OISE

Characterization of cryostat performance $\Big|$ 2

A̶ N essential

2.1 Cooling power

$$P = \dot{Q} = \alpha T_{\mathrm{MXC}}^2 + \beta \qquad (2.1)$$

2.2 Electron temperature

Table 2.1: Mixing chamber temperature for different configurations of anti-reflection (AR) coated windows (Thorlabs WW41050-B) inside the dilution refrigerator (DR).

Windows	T_{MXC} (mK)
None	30.0
Cold	11.0
PT1, PT2, Still	7.9
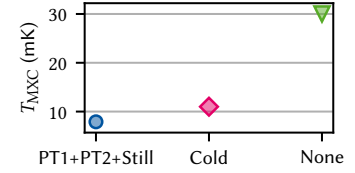
Figure 2.1: Mixing chamber temperature for different configurations of AR coated windows (Thorlabs WW41050-B) inside the DR.
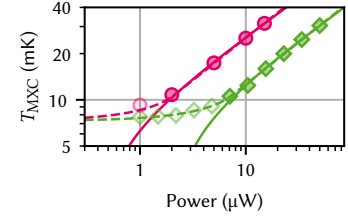
Figure 2.2: Mixing chamber temperature as function of heater (magenta) and laser (green) power. Solid lines are fits to Equation 2.1 including only the solid markers. Green dashed line is a quadratic smoothing spline fit to all laser data points. Magenta dashed line is the laser spline scaled to match the heater data with fitted factor $A = 28\,\%$ corresponding to the fraction of laser power absorbed and non-radiatively emitted.
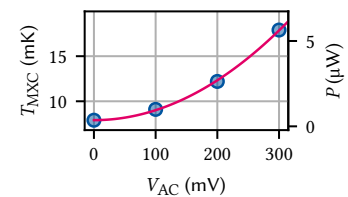
Figure 2.3: Mixing chamber temperature as function of nanopositioner AC readout voltage. Solid line is a fit to $T_{\mathrm{MXC}} = aV_{\mathrm{AC}}^2 + b$. The secondary axis indicates the conversion from T_{MXC} to power obtained in Figure 2.2 which is approximately linear in this regime, leading to the expected $P \sim R^{-1}V_{\mathrm{AC}}^2 \sim$ behav-
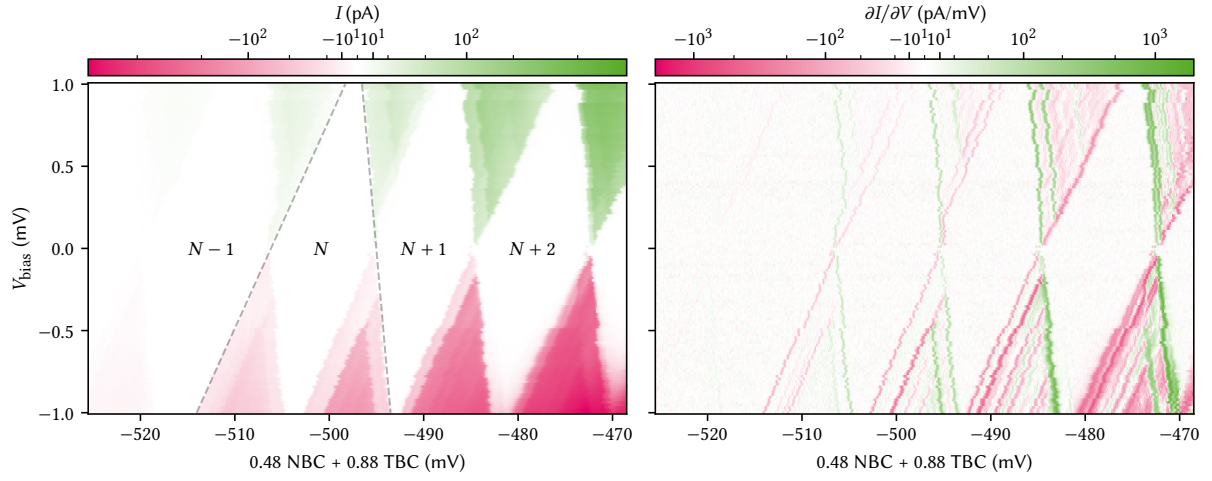
Figure 2.4

Figure 2.5

Figure 2.6

N

3.1 Light coupling

Single-mode fibers (SMFs) are a natural choice to transmit laser light which usually consists of a just that, a single mode. Because the mode profile of SMFs is very close to the fundamental laser mode, TEM_{00}, *Gaussian optics* are required to describe the propagating light.

1. Gaussian optics equations
   a) electric field profile
   b) rayleigh length
   c) beam divergence & diameter

2. diffraction limit
3. numerical aperture (NA)
4. beam diameter
5. choosing lenses

3.1.1 Light collection

In a confocal microscope geometry, light is collected using the same lens that is also used for illumination of the sample. For excitation with a Gaussian laser beam but non-Gaussian radiation profiles being emitted, this means that two different beam behaviors need to be matched, a task that is likely not going to be possible to achieve completely. Since furthermore the emitted light is coupled into a SMF, losses will invariably occur when focusing the non-Gaussian beam onto the SMF acting as a spatial filter. A detailed analysis of the electric field profile to compute t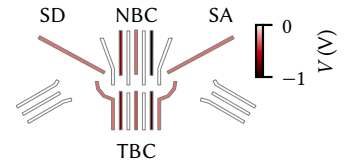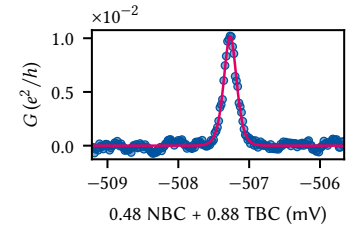he expected coupling efficiency from the sample into the SMF is beyond our scope here. It would require taking into account the full sample and lens geometries as well as diffraction, a task only possible by employing a full-fledged numerical optics simulation suite. However, we can make some crude simplifications of the problem to estimate the order of magnitude of these effects. To this end, I model the light source as a point dipole beneath the surface of a homogeneous slab of dielectric material and the real lenses as ideal thin lenses.

Consider the situation sketched in Figure 3.1. A dipole oriented along x in the plane of a GaAs quantum well (QW) with refractive index n buried at a depth d beneath the surface of the sample emits light into the halfspace above it. The emitted radiation has the electric field distribution

$$E(x, y, z) = E_0 \frac{\exp(ikr)}{r} \cos\theta \qquad (3.1)$$

where $\theta = \arctan x/z$, r is the distance from the point dipole and $k = 2\pi/\lambda = 2\pi n/\lambda_0$ is the wavenumber in the medium.

The emitted light is refracted at the surface and we collect and collimate it with an objective lens (labelled "Ob.") with $\text{NA} = \sin\theta'_m$ at distance f_{ob} above the surface of the sample, where f_{ob} is the focal length and θ'_m
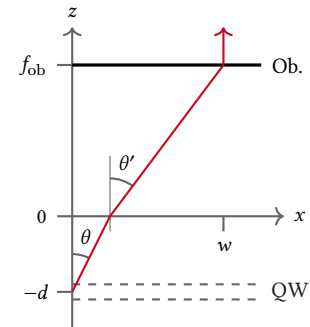

Figure 3.1: Sketch of a light source located inside a dielectric medium ($z < 0, n > 1$) emitting light in the upwards direction to collection by an objective lens in air ($z > 0, n = 1$). The red line indicates the marginal ray of the lens with focal length f_{ob} and clear aperture (CA) $2w$.

the angle of the marginal ray. The NA determines the maximum amount of light the objective lens can collect, and using Snell's law we can relate the angle of a ray outside the sample θ' to the angle inside the sample θ,

$$\sin\theta' = n\sin\theta, \tag{3.2}$$

with $n \approx 3.57$ at $\lambda_0 = 800\,\text{nm}$ and $T = 0\,\text{K}$. This yields $\theta_{\text{m}} = \arcsin(\text{NA}/n) \approx 11°$ for the emission angle of the marginal ray inside the semiconductor, suggesting that Equation 3.1 is well approximated as a spherical wave since $\cos\theta_{\text{m}} \approx 1 - \theta_{\text{m}}^2/2 \approx 1$. Indeed, the fraction of the emitted intensity $I(\theta) \propto |E(\theta)|^2$ being collected by the objective lens, the *collection efficiency*, is

$$
\begin{aligned}
\eta_{\text{c}} &= \frac{\iint_{\theta_{\text{m}}} \mathrm{d}\Omega\, I(\theta)}{\iint \mathrm{d}\Omega\, I(\theta)} \\
&= \frac{\int_0^{\theta_{\text{m}}} \mathrm{d}\theta\, \sin\theta\cos^2\theta}{\int_0^{\pi} \mathrm{d}\theta\, \sin\theta\cos^2\theta} \\
&= \frac{1}{2}\left(1 - \left[1 - \left(\frac{\text{NA}}{n}\right)^2\right]^{3/2}\right)
\end{aligned}
\tag{3.3}
$$

which evaluates to only $\eta_{\text{c}} \approx 2.8\,\%$ for the objective lens's $\text{NA} = 0.7$. Moreover, since $d \sim 100\,\text{nm} \ll f_{\text{ob}} \sim 1\,\text{mm}$ and also $kd \ll 1$, the lateral extent of the light source as viewed from the objective lens is negligibly small and is well approximated by a point source right below the surface.[1]

In order to determine the electric field amplitude as a function of position inside the lens with radius w, consider a light ray impinging on the surface at lateral position x_0. Taking two points of the light ray at $(x_0 - \Delta x, -\epsilon)$ some $\epsilon > 0$ below the surface and $(x_0 + \Delta x', +\epsilon)$ above, we can express the lateral shift due to refraction as

$$\Delta x' = \epsilon\tan\theta' = \Delta x\frac{n\cos\theta}{\sqrt{1 - n^2\sin^2\theta}} \tag{3.4}$$

with $\theta^{(\prime)} = \arctan\left(\Delta x^{(\prime)}/\epsilon\right)$ using standard trigonometric identities. Thus, the coordinate x of the electric field inside the semiconductor transforms to the coordinate x' outside the semiconductor as

$$x \to x' = xn\left[1 + \left(\frac{x}{z}\right)^2 - \left(\frac{nx}{z}\right)^2\right]^{-\frac{1}{2}}, \tag{3.5}$$

which we invert to obtain

$$x = \frac{z}{\sqrt{n^2\left[1 + (z/x')^2\right] - 1}}. \tag{3.6}$$

We now approximate the light source as a point source at $z = -\epsilon < 0$ emitting a spherical wave as discussed above and introduce cylindrical coordinates with $\rho' = \sqrt{x'^2 + y^2}$ so that $r = \sqrt{\rho'^2 + z^2}$. Plugging Equation 3.6 into Equation 3.1 then yields

$$E(\rho', z) = E_0\frac{\exp(ikz\zeta(\rho'))}{z\zeta(\rho')} \tag{3.7}$$

1: Note that I use $f = \text{CA}/2\text{NA}$ rather than the effective focal length quoted by the manufacturer in this section.

with

$$\zeta(\rho') = \sqrt{1 + \left(n^2 \left[1 + (z/\rho')^2\right] - 1\right)^{-1}} \qquad (3.8)$$

for the electric field outside the semiconductor. At the lens $\zeta \approx 1$ so that the field is actually more closely resembled by a plane rather than the original spherical wave.

The radial intensity profile given by the absolute value square of Equation 3.7 is shown in the upper panel of Figure 3.2 together with a flattop (green) and a Gaussian (magenta) beam profile for comparison. The intensity drops only by about 2 % at the edge of the lens aperture, $\rho = w$. We may thus expect non-negligible loss when coupling this beam into a SMF with a guiding mode very closely approximating the Gaussian TEM_{00} mode [1, 2]

$$E(\rho, z) = E_0 \frac{w_0}{w(z)} \exp\left\{-i\left[kz - \arctan\left(\frac{z}{z_0}\right)\right] - \rho^2 \left[\frac{1}{w(z)^2} + \frac{ik}{2R(z)}\right]\right\} \qquad (3.9)$$

with the fiber's mode field diameter (MFD) $2w_0$, the beam's $1/e$-radius

$$w(z)^2 = w_0^2 \left(1 + \frac{z^2}{z_0^2}\right), \qquad (3.10)$$

the wavefront radius of curvature

$$R(z) = z\left(1 + \frac{z_0^2}{z^2}\right), \qquad (3.11)$$

the Rayleigh range

$$z_0 = \frac{\pi w_0^2 n}{\lambda}, \qquad (3.12)$$

and where $z = 0$ in the fiber end face.

The light collected and collimated by the objective lens next passes through the ocular lens in the detection arm which focuses it into the SMF. The image of the beam on the fiber end face is given by the Fraunhofer diffraction pattern generated by the (approximately) plane wave incident on the ocular lens aperture,[2] resulting in the Airy disk [3]

$$E(q) = E_0 2\pi w^2 \frac{\exp(ikf_{\mathrm{oc}})}{f_{\mathrm{oc}}} \frac{J_1(kwq/f_{\mathrm{oc}})}{kwq/f_{\mathrm{oc}}}, \qquad (3.13)$$

where $J_1(x)$ is Bessel function of order one and q the radial coordinate in the image plane, *i.e.*, the fiber end face. Equation 3.13 scaled with the radius ρ is plotted in the middle panel of Figure 3.2 together with the SMF's guiding Gaussian mode. While within the MFD the two modes match quite well, a relevant amount of the power $P(\rho) \propto \int_0^\rho \mathrm{d}\rho' \, \rho' I(\rho')$ resides outside that radius as shown in the bottom panel of the same figure.

The mode matching efficiency is then given by the normalized spatial overlap of the light field (E_l, Equation 3.7) and the fiber's guiding mode (E_f, Equation 3.9) [4],

$$\eta_{\mathrm{m}} = \frac{\int \mathrm{d}S \left|E_f(\rho)\right|^2 \int \mathrm{d}S \left|E_l(\rho)\right|^2}{\left|\int \mathrm{d}S \, E_f(\rho)E_l(\rho)\right|^2} \approx 77\,\% \qquad (3.14)$$

for our parameters.

$I(\rho)/I(0)$

ρ/w

$\rho I(\rho)/(w_0 I(0))$

$P(\rho)/P(\infty)$

ρ/w_0
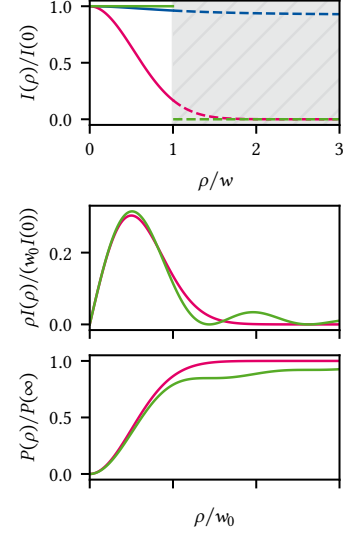
Figure 3.2: Electric field modes. Top: mode intensity of the light collected from the semiconductor at the objective lens plane (blue) in comparison to a flattop (green) and Gaussian TEM_{00} mode with theoretical beam diameter after collimating with the ocular lens. w is the lens CA radius. Middle: diffraction pattern of the collimated beam approximated as a flattop when focusing onto the SMF end face with the ocular lens (green) and the fiber's guiding mode (magenta). The curves are scaled with the radial coordinate ρ to highlight the Airy rings. Bottom: power encased by a circle with radius ρ, $P(\rho) \propto \int_0^\rho \mathrm{d}\rho' \, \rho' I(\rho')$.

2: We can safely neglect diffraction effects from the objective lens aperture. The Fraunhofer criterion b^2/λ with b the aperture diameter is $\approx 30\,\mathrm{m}$, implying the ocular lens at a distance of $\sim 1\,\mathrm{m}$ is in the near field with many Fresnel zones where diffraction does not yet play a significant role [3].

Vibration performance 4

A microscope's performance is limited chiefly by two factors; first and foremost the resolution and imaging fidelity are limited by the systematic aberrations introduced by the optics.[1] Various types of aberrations exist, and modern microscopes usually include a complex assembly of optics to compensate for these errors. The second factor is vibration noise. This becomes more significant the higher the resolution of the microscope simply because ambient, environmental vibrations within the range of human civilization is typically on the order of $100\,\mu m/s$ root mean square (RMS) [5]. Comparing that to transmission electron microscopes with atomic resolution, it is clear that these instruments require purpose-built rooms to reduce the vibration level to acceptable levels.

The demands on the microscope discussed in the present thesis are fortunately much more relaxed as the features we need to resolve are on the micrometer scale. However, we face the additional challenge of ultra-low temperatures, or rather the manner in which they are achieved. The microscope is integrated into a *dry* DR. In contrast to a *wet* DR, which uses a liquid Helium bath, these systems achieve the pre-cooling necessary for the ^{3}He/^{4}He dilution refrigeration cycle to work by adding a secondary refrigeration mechanism, a pulse tube refrigerator (PTR). These are closed-cycle systems that work with ^{4}He compressed to ~21 bar on the high-pressure and ~7 bar on the low-pressure side. A rotating valve connecting high and low pressure lines to the cryostat in turn produces alternating gas flow inside a regenerator, where the gas absorbs heat at the low-temperature and and deposits heat at the high-temperature end [6, 7]. In commercial PTRs the frequency of the pulses of Helium gas, determined by the rotary valve motor, is usually fixed at values around $1.5\,Hz$.

Naturally, the compressor, the rotary valve motor, and the Helium pulses themselves introduce vibrations into the cryostat. While the cold foot of the PTR is not rigidly connected to the cryostat interior,[2] the entire cold head assembly rests with rubber feet on the cryostat top plate in the system's delivery status. Thus, our microscope does not only encounter passive environmental vibrations but also the active perturbation from the PTR.

[9, 10]

review literature

This chapter is laid out as follows. In Section 4.1, I briefly discuss the theoretical underpinnings of vibration isolation to inform its optimization. To characterize and improve upon the isolation, I performed vibration noise spectroscopy using the techniques and tools presented in Part I. I employed two different approaches that I lay out in the following; first, using a commercial piezoelectric accelerometer (Section 4.2) and second, using the optical response of a spatial reflectance gradient (Section 4.3). As will become clear, the two approaches complement each other because they are sensitive to slightly different quantities.

improve

4.1 Vibration isolation

A simple yet effective method of vibration isolation is to suspend the system on passive air springs. These are typically constructed with two separate air chambers, a spring and a damping chamber, connected by pneumatic tubing. The load is rigidly mounted to a plunger that rests on a diaphragm sealing the spring chamber. Excitations of the load induce oscillations in the variable spring chamber volume. The connection to the fixed-volume damping chamber provides a flow impedance[3] that manifests as a damping force to the spring chamber oscillations.

3: The speed of a fluid in laminar flow through a round pipe is proportional to the pressure gradient along the flow direction and to the square of the distance from the wall.

4.1.1 Damping theory

Let us adopt a simple toy model to gain an intuition for the behavior of a mass suspended on air springs as function of vibration frequency by modelling it as a damped harmonic oscillator. Consider the displacement from equilibrium $x(t)$ of the test mass m and switch on an external perturbation $u(t)$ acting on the *base* of the spring, implying that the driving force experiences both the damping rate γ and the spring stiffness $k = m\omega_0^2$ with ω_0 the resonant frequency of the undamped system. We can then compute the transfer function $H(s)$ from the Laplace transform of the Newtonian equation of motion,

$$\ddot{x}(t) + 2\gamma[\dot{x}(t) - \dot{u}(t)] + \omega_0^2[x(t) - u(t)] = 0, \tag{4.1}$$

yielding

$$H(s) = \frac{\hat{x}(s)}{\hat{u}(s)} = \frac{2\gamma s + \omega_0^2}{s^2 + 2\gamma s + \omega_0^2}. \tag{4.2}$$

The magnitude of the transfer function evaluated at $s = i\omega$ is shown in Figure 4.1 for two different dampings, $\gamma = \omega_0/200$ (solid black line) and $\gamma = \omega_0/2$ (dashed black line). Below $\omega = \sqrt{2}\omega_0$ (vertical dotted line), external impulses are in fact amplified. The maximum at the damped system's resonance $\omega_r = [\omega_0^2 - \gamma^2]^{1/2}$ becomes smoothed out and smaller as the damping γ is increased but never drops below unity. This is the reason why resonance frequencies as small as possible are desirable in vibration isolation. Above this frequency, the system initially attenuates with 40 dB per decade up to $\omega = \omega_0^2/(2\gamma)$ and with 20 dB per decade beyond for $\gamma/\omega_0 \to 0$ (the underdamped case). In the strongly damped case ($\gamma/\omega_0 \to \infty$) the attenuation is only 20 dB per decade starting at $\omega = 2\gamma$.

From Equation 4.2 and Figure 4.1, we can infer two possible approaches to isolating a mass from vibrations. The first is to make the system's resonance frequency ω_0 as small as possible by resting it on a spring damping system. This maximizes the region in which external influences are attenuated. The second is to do the opposite, *i.e.*, make the entire system as stiff (large k) and thereby ω_0 as large as possible. While this minimizes the attenuation region, it also moves the amplification region close to the resonance to higher frequencies, and possibly further away from the external excitation. Consequently, this approach makes most sense if it is known that low-frequency excitations are the dominant source of vibrations.

A widely used metric for the isolation demand of vibration-sensitive equipment are the so-called vibration criteria (VCs) [5, 11]. These are
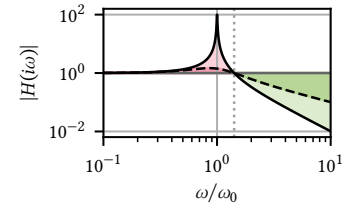
Figure 4.1: Force transmission function of a damped harmonic oscillator with $\gamma = \omega_0/100$ (solid black line) and $\gamma = \omega_0/2$ (dashed black line). Below the break frequency $\omega = \sqrt{2}\omega_0$ (dotted vertical line), external excitations are amplified (shaded red area). For larger damping γ, the amplification at resonance becomes smaller. Above $\omega = \sqrt{2}\omega_0$, excitations are attenuated (shaded green area). Both amplification below and attenuation above the break frequency become smaller as the damping rate γ is increased.

design standard specifications for buildings housing, for example, lithography tools. The vibration criteria (VCs) are defined in terms of band-limited RMS values similar to what I have used in the present thesis (*cf.* Equation 4.4 and **??**). However, instead of computing the band-limited RMS with a fixed lower band edge, one uses bands of a fixed width, typically over one-third of an octave. To be specific, the one-third octave is defined in terms of its midband frequency f_{m} as the interval

$$f \in f_{\mathrm{m}} \times \left[10^{-1/20}, 10^{1/20} \right] \approx f_{\mathrm{m}} \times \left[2^{-1/6}, 2^{1/6} \right] \tag{4.3}$$

whose bandwidth Δf is approximately $26\,\%$ larger than f_{m} and where the latter is defined referenced to 1000 Hz [12]. The criteria, given as velocities rather than displacements or accelerations because it is argued that the limit to photolithography resolution is image velocity, are reproduced from Reference 5 in Table 4.1. For the typical feature sizes we would like our microscope to resolve, the VC-B criterion is a fair target. I will use them below to classify the vibration isolation of the confocal microscope.

4.1.2 Microscope isolation concept

What does this mean for our case of a dry DR? The rotary valve motor of the PTR generates pulses with frequency 1.4 Hz. Commercial damping systems that the space constraints in our lab allow to be accommodated, for example the CFM Schiller MAS 25 [13], have resonance frequencies around $f_0 = 2.5$ Hz, implying the first two harmonics of the PTR excitation fall into the amplification regime as discussed above. We are thus right in-between the two regimes and it is a-priori unclear which isolation scheme to choose without detailed mechanics simulations. Hence, the initial isolation concept for the cryostat envisaged mounting the rotary valve motor rigidly to the stiff aluminium item profile frame, which was additionally filled with sand to increase the system's resonance frequency.

However, prompted by a sudden increase in visually observed vibrations in the microscope image, I modified the cryostat frame to house three air springs [13] in the hopes of isolating the microscope from external disturbances.[4] To this end, I decoupled the frame from which the cryostat itself is suspended from the support frame standing on the lab ground. Extruding from the square footprint of the support frame at two adjacent corners and the center of the diametrically opposite side, the three air springs are mounted with the base on angle brackets connected to the support frame while their plunger is mounted to a second angle bracket connected to the cryostat frame. The springs are connected by pneumatic tubing to a central pressure regulation panel that is connected to the building's central air pressure line. The vertical placement of the springs is chosen such that when the air springs are deflated the cryostat frame rests on the support frame, establishing the same rigid connection that existed previously. This allows examining the influence of the air springs on the vibration isolation without modifying the setup by simply venting the pressurized air from the springs.

In the following, I will characterize the performance of the system with and without the air springs active using two different methods.

Table 4.1: VCs and International Organization for Standardization (ISO) guidelines

1/3 octave band RMS (µm/s)	
Workshop (ISO)	800
Office (ISO)	400
Residential day (ISO)	200
Op. theater (ISO)	100
VC-A	50
VC-B	25
VC-C	12.5
VC-D	6
VC-E	3

[13]: CFM Schiller GmbH (n.d.), *Type MAS*

4: As it turned out, the cause was a damaged nanopositioner bearing rather than environmental. Fortuitiously, the endeavour still proved successful and resulted in an improved vibration performance as I show below.

4.2 Accelerometric vibration spectroscopy

The most straightforward method of measuring vibration noise is an accelerometer. These are devices that convert translational forces, for example by means of a loaded spring, into electrical signals. They are mounted rigidly to the device under test (DUT) and typically connected to some sort of signal conditioner providing a constant current bias to the sensor and putting out a voltage proportional to the acceleration. The most sensitive and low-frequency designs use piezoelectric materials like Quartz crystals for sensitivities in the range of $10\,\mathrm{V}/g$ with a broadband noise floor of $2\,\mu g$ [14].

In order to evaluate the vibration level at the sample position, I designed a small angle bracket onto which the accelerometer[5] can be screwed either in vertical or horizontal direction in the sample puck of the DR, enabling measurements of the displacement noise along the direction of gravity as well as perpendicular to it and the optical axis. The accelerometer is connected to the coaxial cables installed in the cryostat via an adapter cable from imperial 10-32 to SubMiniature version A (SMA) connector. Outside of the cryostat, the signal is routed to a signal conditioner that provides the necessary current bias and outputs a voltage which is digitized by a Keysight 34465A digital multimeter (DMM) connected to the measurement computer. Since the sensor's (conditioned) output is a voltage directly proportional to the acceleration, it is straightforward to compute the displacement power spectral density (PSD) from time series data measured with the DMM using the `python_spectrometer` package presented in **??** [15]. Leveraging the `fourier_procfn` argument, we can transform the voltage data first to acceleration and then, by integration, to displacement in frequency space as indicated in Listing 4.1.

To assess the impact of the PTR and the suspension, I measured the displacement noise PSD for each combination of the two being switched on and off. The cryostat was closed, its vacuum chamber evacuated, and the magnet, a significant seismic mass, mounted as usual. The measurements are shown in Figure 4.2 together with the band-limited RMS (*cf.* **??**),

$$\mathrm{RMS}_S(f) = \sqrt{\int_{f_{\min}}^{f} \mathrm{d}f'\, S^2(f')}. \qquad (4.4)$$

When the PTR is switched off, the spectra with and without suspension are dominated by broadband vibration noise, although quite some structure around 15 Hz, 33 Hz and 60 Hz can be observed.[6] When it is switched on, the PTR pulses at 1.4 Hz and a large number of its higher harmonics visually dominate the spectra. Clearly, the suspension has a larger impact in this case, matching qualitatively the behavior discussed in Section 4.1. At high frequencies, it manages to almost completely suppress the broadband excitation observed without the suspension. At low frequencies, on the other hand, the PTR harmonics are amplified to the degree that the band-limited RMS is dominated by their contribution. Only at around 10 Hz, the attenuation starts to take effect. Overall, the PTR is found to raise the displacement noise RMS amplitude from $0.5\,\mu m$ to $10\,\mu m$ while the suspension, over the entire frequency range, has at best no positive influence.

This result is less than encouraging. At that level of RMS-fluctuations, we'd have a slim chance of resolving micrometer-scale features using the microscope. But is the *absolute* magnitude of displacement noise at

[14]: Wilcoxon Sensing Technologies (n.d.), *731-207 Compact Seismic Accelerometer, 10 V/g*

5: Wilcoxon 731-207 kindly lent by Marcus Eßer [14].

```
from qutil.signal_processing
↪  import fourier_space
from qutil.functools import
↪  chain, scaled
from qutil import const

sensitivity = scaled(1 / 9.9 /
↪  const.g)
fourier_procfn = chain(
    sensitivity,
    fourier_space.derivative
)
```

Listing 4.1: Functionality to transform the conditioned voltage to displacement in Fourier space.

6: Note the curious peaks slightly offset from the second and third harmonic of the PTR frequency in the spectrum with suspension enabled and PTR disabled. We may speculate that these are due to the PTRs of other cryostats in other labs in the vicinity that are transmitted through the floor. Two were running two rooms over at the time the data was acquired.
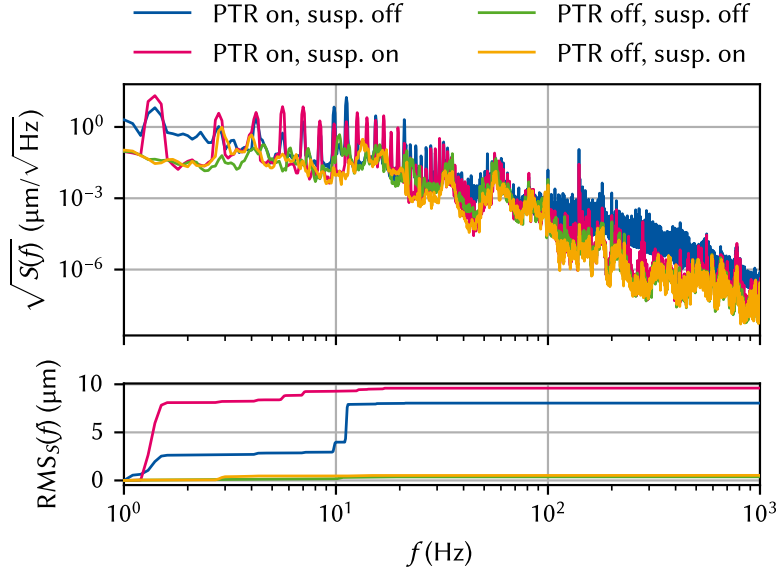
Figure 4.2: Top: displacement noise spectra acquired with the accelerometer at room temperature when the PTR is switched on (blue, magenta) or off (green and orange), and when the air suspension is switched enabled (magenta, orange) or disabled (blue, green). Bottom: band-limited RMS computed from the PSDs in the upper panel (*cf.* **??**). Turning on the PTR increases the RMS noise amplitude by more than an order of magnitude over the entire frequency spectrum. The suspension slightly worsens the total noise because the low-frequency pulses excite the system close to the air springs' resonance frequency of 2.5 Hz.

the sample position really the correct measure for the microscope performance? Indeed, if the sample oscillates in phase with the objective and ocular lenses as well as the SMF, we will still obtain a perfect imaging fidelity. So actually only the *relative* displacements of sample, lenses, and detection fiber affect the achievable resolution of the microscope. To characterize these, I developed an optical *in-situ* technique to measure the displacement noise based on knife-edge reflectance fluctuations that I will present in the following section.

4.3 Optical vibration spectroscopy

The gate electrodes on our samples are fabricated using two separate lithography processes; first, the smallest structures are written using electron-beam lithography (EBL) in two steps. Then, larger structures on the order of 1 μm and above are written using optical lithography. In the region where the two overlap on the mesa to establish electrical contact, the highly reflective Ti/Au optical gates have a width of 14 μm and a height of 160 nm and lie on top of the poorly reflecting GaAs surface, resulting in a step-like reflectance profile. Scanning perpendicularly across such a straight edge between a poorly and a highly reflecting material is known as a knife-edge measurement and is frequently used to measure the spatial extent of a laser spot [16−18]. We can use the same setup to measure the displacement noise; instead of manually shifting our knife edge across the beam spot, though, we measure the reflectance fluctuations induced by the knife edge fluctuating relative to the spot due to external perturbations.

The scenario is sketched in Figure 4.3 in the coordinate system defined by the magnet such that z is along gravity's axis and x is the out-of-plane axis. Focusing the laser (indicated by a dashed circle) onto the edge of the optical gate, we can move the sample using the y-axis nanopositioner and observe a decrease in reflected intensity if the gate is moved away from the laser and an increase if it is moved towards the laser. This gradient in reflected intensity can be inverted to obtain the vibration noise along y by monitoring the intensity as a function of time.
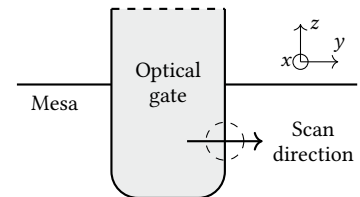

Figure 4.3: Sketch of the region of the sample used for optical vibration spectroscopy. The coordinate system follows the magnet's; z is parallel to gravity, and x is perpendicular to the QW plane. The optical gate extends further north as indicated by the dashed line.

Let us take a closer look at the reflected intensity when the laser spot has a finite overlap with the edge of the gate. Under the simplifying assumption of a perfectly sharp drop-off and taking the reflectance of the Gold gate to be unity, we can write the reflectance as function of the coordinate perpendicular to the gate edge at $y = 0$ as

$$R(y) = \begin{cases} 1, & y \leq 0 \\ r, & y > 0, \end{cases} \tag{4.5}$$

where r is the reflectance of the bare GaAs surface. Assuming a perfect Gaussian (transverse electromagnetic (TEM)$_{00}$ mode) beam characterized by its waist radius w_0 at which the intensity drops to $1/e^2$ of its maximum value, the laser intensity profile in 1D is given by

$$I(y) = I_0 \exp\left(-\frac{2y^2}{w_0^2}\right), \tag{4.6}$$

> is the result the same for 2D? if yes, argue why 1D is sufficient!

where $I_0 = P_0/w_0$ with P_0 the total beam power. The power reflected when the spot partially overlaps with the reflectance step can then be expressed as the convolution

$$P_R(y) = R(y) * I(y) \tag{4.7}$$

$$= \frac{I_0 w_0}{2} \sqrt{\frac{\pi}{2}} \left[1 - (1-r)\,\mathrm{erf}\left(\frac{y\sqrt{2}}{w_0}\right)\right] \tag{4.8}$$

in the yz focal plane, where $\mathrm{erf}(y)$ is the error function.

The function is plotted in Figure 4.4. The contrast that can be achieved is given by $1 - r$. Furthermore, for $y \in [-w_0/2, w_0/2]$ the function is well-approximated by

$$P_R(y) \approx -I_0(1-r)y + \frac{I_0 w_0}{2}\sqrt{\frac{\pi}{2}} \tag{4.9}$$

drawn as a dashed line. Since we measure the photon count rate rather than the power, $\Phi = P\lambda/hc$ with λ the laser wavelength, we rewrite this as

$$\Phi_R(y) = -sy + \frac{\Phi_0}{2}\sqrt{\frac{\pi}{2}}. \tag{4.10}$$

where we defined the *sensitivity*

$$s = \frac{\Phi_0}{w_0}(1-r). \tag{4.11}$$

Hence, to obtain a more sensitive probe for vibrations, meaning that small variations in y lead to large variations in Φ_R, one could either improve the reflectance contrast $1 - r$, decrease the spot size w_0, or increase the incident photon flux Φ_0.[7] In our case, the former two are fixed by the sample and the setup, respectively , whereas the latter is limited by the maximum data transfer rate of the Swabian Instruments Time Tagger 20 counting card, 9 MS/s.

Starting from Equation 4.10, it is straightforward to obtain the displacement in the vicinity of $y = 0$ as function of photon flux,

$$y(\Phi_R) = \frac{w_0}{1-r}\left[\frac{1}{2}\sqrt{\frac{\pi}{2}} - \frac{\Phi_R}{\Phi_0}\right]. \tag{4.12}$$

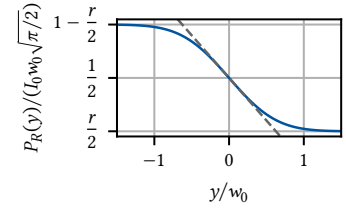To summarize, we can position the laser spot on the edge of an optical

Figure 4.4: Theoretical reflected power for a Gaussian beam of width w_0 and a reflectance contrast of $1 - r$ according to Equation 4.7. The dashed line indicates the leading order approximation at $y = 0$.

7: Note that the smaller w_0, the smaller also the maximum displacement amplitude that can be resolved as the derivative goes to zero as $y \to \pm\infty$.

gate and record a time trace of the photon flux by using the Time Tagger to count the photons detected by the avalanche photodiodes (APDs) mounted on the side exit of the spectrometer. Using Equation 4.12 we can then convert the flux into a displacement and proceed with the usual spectral noise estimation as explained in Part I.

I will now lay out the experimental procedure of calibrating the system to (implicitly) obtain the parameters w_0, r, and Φ_0. The first challenge is obtaining a proper length reference scale. While the nanopositioners on which the sample is mounted do in principle have a resistive position readout, it is extremely unreliable at small displacements. Therefore, I calibrated the relative position using the imaging arm of the optical head. Figure 4.5 depicts the procedure. Illuminating the sample with the white light, I positioned the spot on the edge of the optical gate and imaged the sample with the Thorlabs DCC1545M complementary metal-oxide-semiconductor (CMOS) camera. I then extracted the position of the edge, in pixels, for several rows to obtain some statistics by fitting a linear function to the edge profile in a small region between two refraction maxima. Repeating this step for different DC voltages applied to the nanopositioner, this yields the proportionality factor between the nanopositioner DC voltage, V_{DC}, and the position of the gate edge on the camera. By measuring the total width of the gate on the camera image, I obtained the magnification by referencing it to the design width,

$$M = \frac{w[\text{px}]}{w[\mu\text{m}]} = \frac{116\,\text{px}}{14\,\mu\text{m}} \approx 8.3\,\text{px}/\mu\text{m}. \qquad (4.13)$$

Again performing a linear fit to the data for different voltages then results in the linear transformation from DC voltage to position (upper panel of Figure 4.6).

Lastly, I switched from white light illumination to the laser, focused it onto the edge of a gate, and measured the photon count rate reflected off the sample as a function of V_{DC}, from which we can finally extract the desired sensitivity (slope) $s \approx 2.36(2)\,\text{Mcps}/\mu\text{m}$ of count rate over displacement. The data and fit are shown in the bottom panel of Figure 4.6. Clearly, the count rate is linear in the displacement over a large range, indicating that for fluctuations with amplitude on the order of 100 nm RMS, the measurement sensitivity should be sufficiently robust.

We are now at last able to measure the displacement noise using `python_⌐` `spectrometer`. Setting `procfn` to the linear transformation given in Equation 4.12 and measuring the counts registered by the APDs using the Time Tagger,[8] I obtained the displacement noise PSDs shown in Figure 4.7. A few things stand out. First, rather than the f^{-2} background observed with the accelerometer in Section 4.2, the noise floor is white ($S(f) =$ const.) at approximately $1\,\text{nm}/\sqrt{\text{Hz}}$. To understand why, we need to take a closer look at the counting statistics, which we will postpone for a bit in order to first finish our discussion of the noise spectra. Second, the overall noise level is much – by a factor of 20 RMS – lower than with the accelerometer. We can attribute this to the fact that the optical method is sensitive to relative rather than absolute displacements. If the cryostat and the optical head were infinitely stiff we would measure no displacement noise with this method – intrinsic noise floor notwithstanding – whereas the accelerometer is still sensitive to oscillations of the cryostat on the air spring fulcrum. In that sense the optical method gives us the more pertinent results because only the displacements seen by the light travelling through the microscope ultimately matter. Third, in contrast to the accelerometer measurements, the RMS amplitude is reduced by
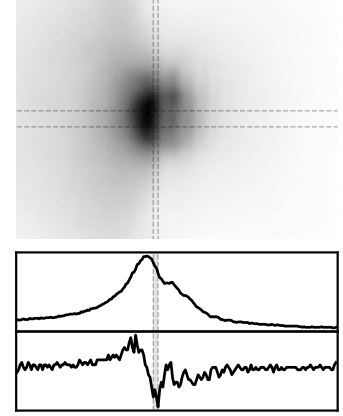

Figure 4.5: Calibration of the length reference scale. The top shows a CMOS camera image (higher intensity darker) of the white light spot on the edge of the optical gate as indicated in Figure 4.3. Several diffraction lines can be seen parallel to the edge. The vertical dashed lines indicate the region in which the intensity slope was fitted. The horizontal dashed lines indicate the extent of rows averaged over. The lower plots show a line cut along the central row of the considered region (top) and its derivative (bottom).
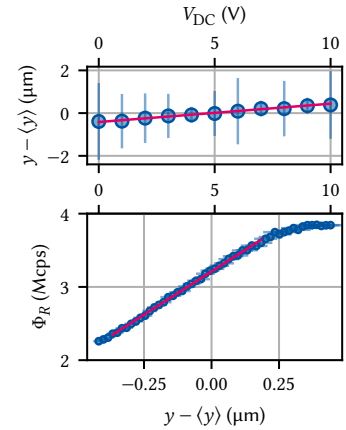

Figure 4.6: Top: linear fit of the edge positions extracted from the analysis in Figure 4.5. Error bars are propagated standard errors of the weighted average of edge positions extracted from different rows. Bottom: laser photon count rate as function of position set by the nanopositioner. Fitting the region $V_{DC} \in [0.5, 7]\,\text{V}$ yields $s \approx 2.36(2)\,\text{Mcps}/\mu\text{m}$ (*cf.* Equation 4.10). Error bars on Φ_R show the standard error of the mean over multiple observations and error bars on y show the fit error from the top panel.

8: Since the APDs are arranged in a Hanbury Brown-Twiss (HBT) geometry, I combined the counts of both instruments using the virtual channel functionality of the Time Tagger.
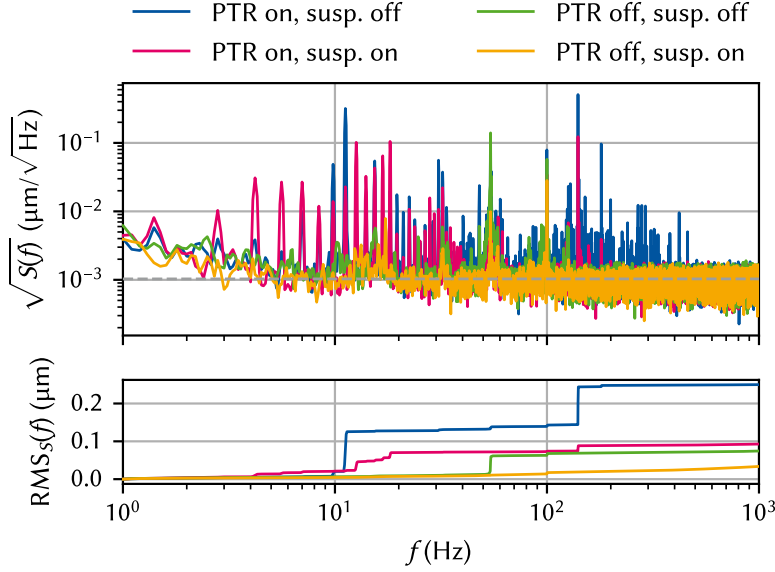
Figure 4.7: Top: displacement noise spectra acquired with the optical *in-situ* method at room temperature when the PTR is switched on (blue, magenta) or off (green and orange), and when the air suspension is switched enabled (magenta, orange) or disabled (blue, green). The dashed gray line indicates the theoretical noise floor derived in Subsection 4.3.1. Bottom: band-limited RMS computed from the PSDs in the upper panel (*cf.* **??**). The PTR has a much smaller effect than when measuring the absolute displacement noise with the accelerometer, increasing the RMS only by a factor of two. While the lowest-order PTR harmonics are amplified by up to an order of magnitude in amplitude with the suspension enabled, they contribute relatively little to the total RMS and are compensated by the superior high-frequency attenuation behavior. The total $\mathrm{RMS}_S \approx 100\,\mathrm{nm}$ with the cryostat in operation is below the typical μm feature size.

half when the suspension is active. Although the harmonics of the PTR frequency of 1.4 Hz are again amplified by the suspension below 10 Hz, raising the band-limited RMS above that with the suspension disabled, there occurs a crossover at the eighth harmonic frequency beyond which the attenuation outweighs the amplification at low frequency.[9]

4.3.1 Noise floor

The noise floor in the optical vibration measurements shown in Figure 4.7 is qualitatively very different from that observed with the accelerometer. There, the *acceleration* noise floor was white,[10] whereas with the optical method the *displacement* noise floor is white, hinting at a different underlying mechanism.

To elucidate this issue, we model the detection event of a single photon (a "click") arriving at the detector at a random time t_i as a δ-function so that the total flux as function of time is given by

$$\Phi(t) = \sum_i \delta(t - t_i). \qquad (4.14)$$

Assuming them to be uncorrelated, the time difference between subsequent clicks is exponentially distributed with average rate $\bar{\Phi}$, $|t_{i+1} - t_i| \sim \mathrm{Exp}(\bar{\Phi})$ [19]. From this it follows that the number of clicks $N(\Delta t)$ within a given time bin $t \in [s, u]$ of length $\Delta t = |u - s|$ is Poisson distributed, $N(\Delta t) \sim \mathrm{Pois}(\bar{N})$, with mean number of counts $\langle N(\Delta t) \rangle = \bar{N} = \bar{\Phi}\Delta t$ [20]. Using the formalism developed in **??**, we can now compute the PSD of the stochastic process $\delta N(\Delta t) = N(\Delta t) - \bar{N}$. To this end, observe that because we assumed arrivals to be uncorrelated, $N_{u'}(\Delta t)$ for a time bin starting at $t = u'$ is independent of $N_{s'}(\Delta t)$ for a time bin starting at $t = s'$. In other words, the autocorrelation function of $\delta N(\Delta t)$ is nonzero only for the same time bins,

$$C_{\delta N(\Delta t)}(\tau) = \left\langle (N_s(\Delta t) - \bar{N})(N_u(\Delta t) - \bar{N}) \right\rangle = \mathrm{Var}(N(\Delta t))\delta(\tau), \qquad (4.15)$$

where $\tau = s' - u'$ and $\delta(\tau)$ is to be understood in a broad sense as zero if $|\tau| > \Delta t$ and $1/2\Delta t$ else. For the Poisson distribution the variance is equal

9: It furthermore appears that even a measurement whose sole electronic device is a picosecond-resolution counting card cannot escape 50 Hz power line noise (or in this case its second harmonic).

10: Remember that as acceleration is the second time derviative of displacement, in frequency space it is proportional to f^2 times the latter.

to its mean so that we obtain

$$C_{\delta N(\Delta t)}(\tau) = \bar{N}\delta(\tau). \tag{4.16}$$

In the limit of $\Delta t \to 0$, we can then perform the Fourier transform to obtain the PSD of $\delta N = \lim_{\Delta t \to 0} \delta N(\Delta t)$,[11]

$$S_{\delta N}(\omega) = \bar{N}, \tag{4.17}$$

that is, δN is a white noise without frequency dependence.[12] $S_{\delta N}$ can be seen as the *instantaneous* number noise PSD.

As a last step, we consider once again discretely sampling the *continuous* process δN with PSD $S_{\delta N}(\omega)$ at rate $f_s = \Delta t^{-1}$ in order to find an expression for the PSD of the discrete process $\delta N(\Delta t)$, $S_{\delta N(\Delta t)}(\omega)$. We know from above that $\mathrm{Var}(\delta N(\Delta t)) = \bar{N}$. On the other hand, recall from **??** that also

$$\mathrm{Var}(\delta N(\Delta t)) = \int_{-\infty}^{\infty} \frac{\mathrm{d}\omega}{2\pi} S_{\delta N(\Delta t)}(\omega) = \int_{-f_s/2}^{f_s/2} \mathrm{d}f\, S_{\delta N(\Delta t)}(f) \tag{4.18}$$

where the last equation holds true because of the finite bandwidth of the discretely sampled signal. Since $S_{\delta N}$ is white, it follows that $S_{\delta N(\Delta t)}$ is, too, and we can directly evaluate Equation 4.18, obtaining[13]

$$S_{\delta N(\Delta t)}(\omega) = \frac{\bar{N}}{f_s}. \tag{4.19}$$

To convert to the displacement noise PSD, we can simply convert units using the calibration derived above because if $N \sim \mathrm{Pois}(\bar{N})$ then so $y \sim \mathrm{Pois}(\bar{N}f_s/s)$ where s is the slope of the calibration converting displacements to count rates, *i.e.*, the sensitivity (see Figure 4.6 and Equation 4.10). Hence,[14]

$$S_{\delta y(\Delta t)}(\omega) = \frac{\bar{N}}{f_s} \times \left(\frac{f_s}{s}\right)^2 = \frac{\bar{\Phi}}{s^2} \tag{4.20}$$

with $\delta y = y - \langle y \rangle$. This type of noise is known as *shot noise*. It was first studied in the context of electron transport by Schottky [21] and results from the discrete nature of, in our case, photons and their stochastic emission times [22]. For the parameters in the present measurements, $\bar{\Phi} \approx 3\,\mathrm{Mcps}$ and $s \approx 2.36\,\mathrm{Mcps/\mu m}$ (*cf.* Figure 4.6), we obtain a shot noise floor of $S_{\delta y(\Delta t)} \approx 1\,\mathrm{nm}/\sqrt{\mathrm{Hz}}$ in excellent agreement with the data shown in Figure 4.7 where the theoretical value is indicated by a gray dashed line.

Inserting the theoretical expectation for the sensitivity s, Equation 4.11, into Equation 4.20, we find that

$$S_{\Delta y(\Delta t)}(\omega) = \frac{\epsilon}{\Phi_0}\left(\frac{w_0}{1-r}\right)^2 \tag{4.21}$$

if we identify $\bar{\Phi} = \epsilon\Phi_0$ for some (fixed) setup efficiency ϵ. This shows a clear path towards improving the signal-to-noise ratio (SNR) of the method. Just as the sensitivity s is improved by increasing $\bar{\Phi}$ and $1 - r$ and by decreasing w_0, so is the shot noise floor, albeit *quadratically* in w_0 and $1 - r$. For example, for a reduction in spot size by a factor of two from inserting a different objective lens and a tenfold increase in maximum count rate achieved by replacing the counting card with a more

11: Despite appearances, $S_{\delta N}$ has units $\mathrm{cts}^2/\mathrm{Hz}$. The discrepancy stems from the difficulty in defining a continuous white noise process.

12: Note that we could have also arrived at this result directly by computing the autocorrelation function $\langle \delta N(t)\delta N(t-\tau)\rangle$ from Equation 4.14 with $N(t) = \int \mathrm{d}t\,\Phi(t)$.

13: $S_{\delta N(\Delta t)}$ also has units $\mathrm{cts}^2/\mathrm{Hz}$.

14: Note that this is the two-sided PSD; to convert to the one-sided version used in this chapter, multiply by two.

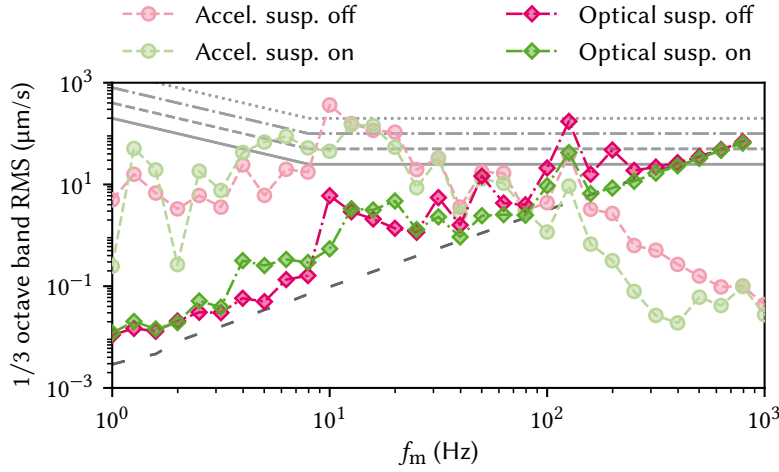powerful model,[15] our simple model predicts a noise floor of 25 pm/$\sqrt{\mathrm{Hz}}$, a reduction by a factor of 40.

To conclude this section, let us come back to the vibration criteria defined in Subsection 4.1.1 and evaluate the microscope based on the two different measurement methods presented in this chapter. The 1/3 octave band RMS velocities computed for the vibration spectra with PTR enabled shown in Figures 4.2 and 4.7 are plotted in Figure 4.8. Based on the data from the accelerometer (circles), the microscope does not meet the targeted level of vibration isolation (VC-B, solid gray line) over three octaves. Because this method of measuring the vibration noise is sensitive to absolute changes, we can understand qualitatively why this is the case if we view the accelerometer at the sample position as the end of a large pendulum whose fulcrum is in the center of the plane spanned by the three air springs. A rough estimate gives a resonant frequency of 0.5 Hz,[16] implying frequencies in the considered range, [4, 32] Hz, are fairly effective at exciting motion in the pendulum (*cf.* Subsection 4.1.1). By contrast, with the optical method we do not pick up on such motion because the ocular lens focusing the light into the SMF is fixed in the co-rotating frame with respect to our imagined pendulum. Indeed, the VC velocities computed for this method show that they are orders of magnitude smaller at low frequencies in particular since only deviations from the rigid body picture established above induce a change in signal. Furthermore, the RMS is dominated by the broadband shot noise floor indicated by the loosely dashed dark gray line, implying that the true vibration-induced RMS is well below our targeted VC-B criterion.

4.4 Routes for improvement

Several improvements could be made to the system if the external conditions would allow it. First, the rotary valve motor should be moved further away from the cold head.[17] As per the initial installation status, it is currently connected to the cold head with a flexible hose at a right angle and a distance of roughly 50 cm, which is below the minimum bend radius recommended by Oxford Instruments.[18] Additionally, the term "flexible" is relative here given the pressure of 20 bar. Increasing the length of the hose should reduce its relative rigidity and thereby its ability to transmit vibrations from the motor to the cold head.

15: Swabian Instruments offers models with up to 1.2 GS/s, although at that rate the jitter and dead time of the APDs would start to become the limiting factors [23].

16: The center of mass sits close to the magnet approximately l = 1 m below the springs so that we have $f = (2\pi)^{-1}\sqrt{g/l} \approx 0.5$ Hz.

17: Clearly, this will impact the performance of the PTR to some extent and should therefore be considered carefully.

18: Note that the orientation of the motor, which is horizontal with the axis, is also not the recommended configuration.

Next, the cold head should be mounted firmly to a secondary reference frame, for instance the ceiling or the lower cryostat frame on which the springs rest. An intuitively obvious step, it has also been shown in the literature that decoupling the PTR from the cryostat in this fashion leads to significant improvements in vibration isolation [24].[19] Acoustic insulation of the room and PTR flex hoses could further improve the low-frequency response of the system [25, 26]. Lastly, let me note that there also exist cryocoolers with variable operating frequency that can thus be tuned away from problematic resonances in the system [27].

In Appendix A, I show additional spectroscopy data, including data measured along the gravitational axis in the puck and on the floor of different rooms, which suggests moving to a different laboratory could also benefit the vibration stability, as well as data for different configurations of the PTR motor.

19: The former option was attempted, but showed no clear improvements in the measurements for reasons unclear, see Appendix A for additional data. It did emphatically deteriorate the inter-departmental atmosphere. Apologies to the institute on the floor above.
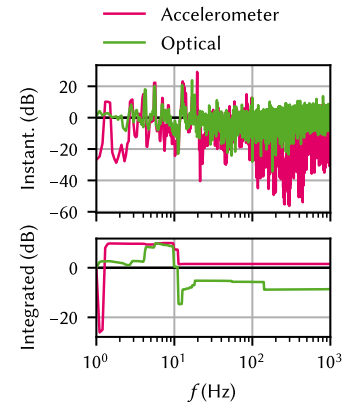
appendix plots

Conclusion & outlook | 5

N OISE

Figure 5.1:

Part III

Optical Measurements of Electrostatic Exciton Traps in Semiconductor Membranes

Part IV

A Filter-Function Formalism For Unital Quantum Operations

APPENDIX

Additional vibration spectroscopy data A

Bibliography

[1] Amnon Yariv. *Quantum Electronics*. 3. ed. New York: Wiley, 1989. 676 pp. (cited on page 8).

[2] Jr. Kowalevicz, Bucholtz Andrew M., and Frank. *Beam Divergence from an SMF-28 Optical Fiber*. Fort Belvoir, VA: Defense Technical Information Center, Oct. 6, 2006. DOI: `10.21236/ADA456331`. (Visited on 07/31/2023) (cited on page 8).

[3] Eugene Hecht. *Optics*. 5 edition. Global edition. Boston: Pearson Education, Inc, 2017. 1 p. (cited on page 8).

[4] Dr Rüdiger Paschotta. "Mode Matching." In: *RP Photonics Encycl.* (Apr. 20, 2005). (Visited on 05/25/2025) (cited on page 8).

[5] Colin G. Gordon. "Generic Vibration Criteria for Vibration-Sensitive Equipment." In: *Optomech. Eng. Vib. Control.* Optomechanical Engineering and Vibration Control. Vol. 3786. SPIE, Sept. 28, 1999, pp. 22–33. DOI: `10.1117/12.363802`. (Visited on 10/14/2022) (cited on pages 9–11).

[6] Ray Radebaugh. "Cryocoolers: The State of the Art and Recent Developments." In: *J. Phys.: Condens. Matter* 21.16 (Mar. 2009), p. 164219. DOI: `10.1088/0953-8984/21/16/164219`. (Visited on 05/01/2025) (cited on page 9).

[7] A. T. A. M. de Waele. "Basic Operation of Cryocoolers and Related Thermal Machines." In: *J Low Temp Phys* 164.5 (Sept. 1, 2011), pp. 179–236. DOI: `10.1007/s10909-011-0373-x`. (Visited on 05/01/2025) (cited on page 9).

[8] Cryoconcept. *1-HEXA-DRY M.* URL: `https://cryoconcept.com/product/hexa-dry-m/` (visited on 05/02/2025) (cited on page 9).

[9] S. Caparrelli et al. "Vibration-Free Cryostat for Low-Noise Applications of a Pulse Tube Cryocooler." In: *Review of Scientific Instruments* 77.9 (Sept. 19, 2006), p. 095102. DOI: `10.1063/1.2349609`. (Visited on 05/02/2025) (cited on page 9).

[10] M. Pelliccione et al. "Design of a Scanning Gate Microscope for Mesoscopic Electron Systems in a Cryogen-Free Dilution Refrigerator." In: *Review of Scientific Instruments* 84.3 (Mar. 12, 2013), p. 033703. DOI: `10.1063/1.4794767`. (Visited on 05/02/2025) (cited on page 9).

[11] Colin G. Gordon. "Generic Criteria for Vibration-Sensitive Equipment." In: *Vib. Control Microelectron. Opt. Metrol.* Vibration Control in Microelectronics, Optics, and Metrology. Vol. 1619. SPIE, Feb. 1, 1992, pp. 71–85. DOI: `10.1117/12.56826`. (Visited on 05/09/2025) (cited on page 10).

[12] American National Standards Institute and Acoustical Society of America. *ANSI/ASA S1.11-2004 (R2009) - Octave-Band and Fractional-Octave-Band Analog and Digital Filters.* URL: `https://webstore.ansi.org/Standards/ASA/ansiasas1112004r2009` (visited on 10/14/2022) (cited on page 11).

[13] CFM Schiller GmbH. *Type MAS.* URL: `https://www.cfm-schiller.de/en/vibration-isolation-technology/products/luftfedern/type-mas/` (visited on 05/02/2025) (cited on page 11).

[14] Wilcoxon Sensing Technologies. *731-207 Compact Seismic Accelerometer, 10 V/g.* URL: `https://wilcoxon.com/731-207/` (visited on 05/02/2025) (cited on page 12).

[15] Tobias Hangleiter et al., *Python-Spectrometer* version 2024.11.1, Nov. 21, 2024. Zenodo. DOI: `10.5281/ZENODO.13789861` (cited on page 12).

[16] J. A. Arnaud et al. "Technique for Fast Measurement of Gaussian Laser Beam Parameters." In: *Appl. Opt., AO* 10.12 (Dec. 1, 1971), pp. 2775–2776. DOI: `10.1364/AO.10.002775`. (Visited on 05/05/2025) (cited on page 13).

[17] D. R. Skinner and R. E. Whitcher. "Measurement of the Radius of a High-Power Laser Beam near the Focus of a Lens." In: *J. Phys. E: Sci. Instrum.* 5.3 (Mar. 1972), p. 237. DOI: `10.1088/0022-3735/5/3/015`. (Visited on 05/05/2025) (cited on page 13).

[18] John M. Khosrofian and Bruce A. Garetz. "Measurement of a Gaussian Laser Beam Diameter through the Direct Inversion of Knife-Edge Data." In: *Appl. Opt., AO* 22.21 (Nov. 1, 1983), pp. 3406–3410. DOI: `10.1364/AO.22.003406`. (Visited on 05/05/2025) (cited on page 13).

[19] *Exponential Distribution.* In: *Wikipedia.* Apr. 15, 2025. (Visited on 05/07/2025) (cited on page 16).

[20] *Poisson Distribution.* In: *Wikipedia.* Apr. 26, 2025. (Visited on 05/07/2025) (cited on page 16).

[21] W. Schottky. "Über spontane Stromschwankungen in verschiedenen Elektrizitätsleitern." In: *Annalen der Physik* 362.23 (Jan. 1918), pp. 541–567. DOI: `10.1002/andp.19183622304`. (Visited on 05/07/2025) (cited on page 17).

[22] Ya. M. Blanter and M. Büttiker. "Shot Noise in Mesoscopic Conductors." In: *Physics Reports* 336.1 (Sept. 1, 2000), pp. 1–166. DOI: `10.1016/S0370-1573(99)00123-4`. (Visited on 05/06/2025) (cited on page 17).

[23] Swabian Instruments. *Time Tagger Series.* URL: `https://www.swabianinstruments.com/time-tagger/` (visited on 05/10/2025) (cited on page 18).

[24] E. Olivieri et al. "Vibrations on Pulse Tube Based Dry Dilution Refrigerators for Low Noise Measurements." In: *Nuclear Instruments and Methods in Physics Research Section A: Accelerators, Spectrometers, Detectors and Associated Equipment* 858 (June 2017), pp. 73–79. DOI: `10.1016/j.nima.2017.03.045`. (Visited on 08/15/2022) (cited on page 19).

[25] D. Schmoranzer et al. "Cryogenic Broadband Vibration Measurement on a Cryogen-Free Dilution Refrigerator." In: *Cryogenics* 98 (Mar. 1, 2019), pp. 102–106. DOI: `10.1016/j.cryogenics.2019.01.010`. (Visited on 05/02/2022) (cited on page 19).

[26] Seong Woo Oh et al. "Cryogen-Free Scanning Gate Microscope for the Characterization of Si/Si$_{0.7}$Ge$_{0.3}$ Quantum Devices at Milli-Kelvin Temperatures." In: *AIP Advances* 11.12 (Dec. 21, 2021), p. 125122. DOI: `10.1063/5.0056648`. (Visited on 05/02/2025) (cited on page 19).

[27] TransMIT. *Two Stage Pulse Tubes.* URL: `https://cryo.transmit.de/en/products/two-stage-pulse-tubes` (visited on 05/05/2025) (cited on page 19).

Special Terms

A
APD avalanche photodiode. 15, 18
AR anti-reflection. 4

C
CA clear aperture. 6–8
CMOS complementary metal-oxide-semiconductor. 15

D
DMM digital multimeter. 12
DR dilution refrigerator. 4, 9, 11, 12
DUT device under test. 12

E
EBL electron-beam lithography. 13

H
HBT Hanbury Brown-Twiss. 15

I
ISO International Organization for Standardization. 11, 18

M
MFD mode field diameter. 8
MXC mixing chamber. 4

N
NA numerical aperture. 6, 7

P
PSD power spectral density. 12, 13, 15–17
PT1 first pulse tube stage. 4, 9
PT2 second pulse tube stage. 4, 9
PTR pulse tube refrigerator. 9, 11–13, 16, 18, 19

Q
QW quantum well. 6, 13

R
RMS root mean square. 9, 11–13, 15, 16, 18

S
SMA SubMiniature version A. 12
SMF single-mode fiber. 6, 8, 13, 18
SNR signal-to-noise ratio. 17

T
TEM transverse electromagnetic. 6, 8, 14

V
VC vibration criterion. 10, 11, 18